Article

Hybrids of Reduced Graphene Oxide Aerogel and CNT for Electrochemical O₂ Reduction

Javier Hernández-Ferrer [ID], Ana M. Benito [ID], Wolfgang K. Maser [ID] and Enrique García-Bordejé *[ID]

Instituto de Carboquímica (ICB-CSIC), Miguel Luesma Castán 4, E-50018 Zaragoza, Spain;
Jhernandez@icb.csic.es (J.H.-F.); abenito@icb.csic.es (A.M.B.); wmaser@icb.csic.es (W.K.M.)
*   Correspondence: jegarcia@icb.csic.es; Tel.: +34-976-733-977; Fax: +34-976-733-318

Abstract: Carbon nanotubes (CNTs), graphene aerogels (GAs), and their hybrid (CNT-GA) prepared by hydrothermal treatment were tested in the electrocatalytic oxygen reduction reaction (ORR). The importance of porous structure derived from the combination of mesoporosity coming from CNTs with macroporosity stemming from GAs was evidenced because the hybrid carbon material exhibited synergistic performance in terms of kinetic current and onset potential. Different electrocatalysts were prepared based on these hybrids doped with nitrogen using different precursors and also supporting Fe nanoparticles. N-doped carbon hybrids showed higher electrocatalytic activity than their undoped counterparts. Nevertheless, both doped and undoped materials provided a mixed two and four electron reduction. On the other hand, the addition of a Fe precursor and phenanthroline to the CNT-GA allowed preparing an N-doped hybrid containing Fe nanoparticles which favored the 4-electron oxygen reduction to water, thus being an excellent candidate as a structured cathode in fuel cells.

1. Introduction

The electrochemical oxygen reduction reaction (ORR) can occur either involving four electrons yielding water (Equation (1)) or involving two electrons producing hydrogen peroxide (Equation (2)). Both reactions have a high impact on current society, the first for fuel cell development and the second for hydrogen peroxide (H₂O₂) production, which is among the 100 most important chemicals in the world. A catalyst with high activity and high selectivity towards the 4e⁻ reduction is needed to overcome the sluggish ORR kinetics occurring at the cathode of a fuel cell [1,2]. Regarding selectivity, the O₂ reduction with 2e⁻ is detrimental for fuel cell performance because reduces its efficiency and the produced H₂O₂ damages the membrane fuel cell [3]. Nevertheless, high selectivity to 2e⁻ reduction is desired for decentralized H₂O₂ production as an alternative to the established industrial anthraquinone process [4,5]. Most of the ORR catalysts are not purely selective to the two or the four electron reduction, but they involve a combination of both mechanisms Equations (1) and (2). Therefore, cheap catalysts delivering high selectivity and activity to one of the two processes are of high technological interest.

$$O_2(g) + 4H^+ + 4e^- \rightarrow 2H_2O(l) \; E_0 = 1.229 \text{ V} \tag{1}$$

$$O_2(g) + 2H^+ + 2e^- \rightarrow H_2O_2(aq) \; E_0 = 0.682 \text{ V} \tag{2}$$
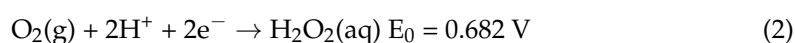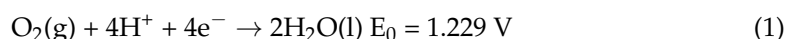
Currently, noble metals or their alloys are the most efficient electrocatalysts both for fuel cell cathodes and for H₂O₂ production [6,7]. However, the scarcity and high price of noble metal hinder their large-scale application. In recent decades, the research has focused on the development of earth-abundant materials to substitute the expensive and scarce platinum-loaded carbon [8]. Carbon materials have shown high promise as metal-free

electrocatalysts for O_2 reduction, as they are earth-abundant, highly tunable, and stable under reaction conditions [1,2,9]. Recent studies have demonstrated that their activity is correlated to the carbon structure and heteroatom doping [10]. Among them, nitrogen doped carbons have been widely investigated. Their unique electronic properties are derived from the conjugation between the orbitals of the nitrogen lone-pair of electrons and the graphitic π-system. Different carbon materials doped with nitrogen have shown high selectivity to either H_2O [10–13] or H_2O_2 [14–19]. The reasons that govern the selectivity are still elusive, hampering a rational catalyst design. Besides the N-doping type, other factors such as the microstructure of carbon or the porous structure are also reported to affect the selectivity towards a certain product. For instance, it is reported that a carbon material with an open structure such as carbon nanohorns [16] or mesoporous carbon [17] favours the desorption of H_2O_2 preventing subsequent reduction to H_2O.

N-doped carbon black or activated carbons have been frequently utilized as electro-catalysts due to their high availability, high surface area, and low cost [20,21]. However, insufficient electrochemical stability due to the abundance of defects and low catalyst utilization due to hindered transport of electrolyte, O_2, and products in micropores have spurred the research about alternative carbon materials [22–25]. Catalyst supports that consist of a highly graphitized carbon structure, such as carbon nanotubes (CNTs) and graphene, are reported to be highly stable under electrochemical conditions [2]. One strategy to increase active site exposure is the 3D structuring of carbon materials [26]. Graphene has high conductivity and can be doped by heteroatoms. However, it tends to restack leading to low porous and high compact materials similar to pristine graphite [27]. To prevent restacking of graphene, several approaches have been used, such as using freeze-drying to form aerogels [28] or forming hybrids with CNTs, which function as spacers for graphene sheets [29]. In graphene-CNT hybrid, the CNTs form a conductive framework to which the graphene flakes adhere, significantly improving the overall conductivity with respect to CNT alone due to an increase in tunnelling efficiency [30,31]. In our previous work, hydrothermal treatment of GO dispersion led to porous reduce graphene oxide hydrogel and subsequently aerogel after freeze drying [32,33]. In the literature, there are a few examples of the preparation of graphene-CNT used for supercapacitors [29] and metal-free ORR catalysts [34]. In this latter work graphene- CNT showed enhanced performance in 4 electron reduction ascribed to the N-doping but the porosity was not characterised. Herein, we have prepared graphene-CNT hybrid aerogels. They have been doped with nitrogen either in one-pot or ex situ. N-doped CNT-GA hybrid was also loaded with Fe nanoparticles in a one-pot hydrothermal process using Fe precursor and phenanthroline as chelating agent and N-precursor. We have analysed the performance of the different doped and undoped GA-CNT hybrid materials in the electrochemical oxygen reduction reaction (ORR) and also elucidated the effect of the porous structure of the hybrid (GA-CNT) compared to the single components.

2. Results and Discussion

Carbon materials are reported to have intrinsic electrochemical activity. For instance, the electrochemical activity of pristine heteroatom-free CNT is attributed to its quantum properties that enhance charge transfer via the electron tunnelling under the electrochemical polarization potential driving force [35]. Here, we studied the electrocatalytic activity of carbon materials such as carbon nanotubes (CNT), graphene aerogels (GA), and their hybrids (GA-CNT) with different CNT contents in electrochemical ORR by linear sweep voltammetry experiments (Figure 1a). The carbon materials have activity in the ORR reaction but exhibit only modest current values (<-2.5 mA cm^{-2}). The activity of carbon materials can be attributed either to the defects on the graphitic lattice or to oxygenated groups. On one hand, the topological defects break the delocalization of electrons and promote the O_2 chemisorption and electrocatalytic reduction [36,37]. The catalytic activity of defects has been reported both for CNT [37] and for graphene [38]. On the other hand, oxygenated groups change the electron density of carbon, which promotes O_2 adsorption

at certain sites [39]. Moreover, oxygenated groups on carbon make it hydrophilic benefiting the diffusion of the electrolyte and O_2 [40]. In our case, the raw materials are oxidised CNT and GO containing both types of active sites. After hydrothermal treatment CNT and GA still contain some oxygenated groups as demonstrated by elemental analysis (Table 1). Moreover, GA also contains nitrogen that comes from the addition of NH_3 during the preparation step, which can contribute to its activity. However, the nitrogen content of GA does not supply a larger kinetic current and number of electrons than nitrogen-free CNT, which can be attributed to the higher conductivity of the latter. In general, the CNT-GA hybrid shows a synergistic effect leading to a slightly more positive onset potential than the single components. However, it varies depending on the amount of CNTs and on the presence/absence of the thermal treatment step. The main parameters derived from polarization curves (Figure S2 of Supplementary Material) are compared in Figure 1b–d. For the lowest concentrations of CNTs (5 and 10 mg), the onset potential and kinetic currents are higher for the as-synthesised sample than for the pyrolysed one which can be attributed to the larger content of heteroatoms (O, N) in the hybrid before pyrolysing. However, the number of electrons does not change, remaining at around 2.5. When the CNT content increased to 15 and 20 mg, the performance in terms of onset potential, kinetic current, and number of electrons worsens for the as-synthesised catalysts but it is enhanced for the pyrolysed ones. Consequently, for high CNT content catalysts, the pyrolysed samples outperforms the pristine counterpart in terms of onset potential and number of electrons, reaching the highest value (2.9 electrons) among all only-carbon catalysts. It can be argued that for high CNT content the pyrolysis treatment favours the electronic interaction between GA and CNT. In principle, pyrolysis at 700 °C may have some favourable effects for ORR, namely, it can create more active defects by removal of oxygen as CO_2, remove the more acidic oxygenated groups, leave more basic groups, which are reported to be more active in ORR [39], and transform amines to pyridinic, pyrrolic, or quaternary nitrogen. However, the favourable effect of pyrolysis is not appreciable for low CNT contents presumably due to the insufficient electric connection between graphene sheets.

**Table 1.** Elemental analysis of different materials.

Catalyst	C wt%	O wt%	N wt%	H wt%
CNT	93.7	5.1	0.6	0.6
GA	70	21.1	8.3	0.9
GA-CNT	81.8	13	4.4	0.8
CNT_700	97.6	1.6	0.4	0.4
GA_700	83	7.9	8	0.8
GA-CNT_700	90.4	4.8	4.2	0.6

Besides the active sites such as heteroatoms or defects, other factors can affect the electrochemical behaviour of carbon materials such as electrically conductive pathways and porosity. This latter may affect the accessibility of electrolyte and the diffusion of O_2 and intermediate products (mainly H_2O_2) to/from the catalytic sites. Therefore, the texture of the carbon materials (CNT, GA, and GA-CNT hybrids) was characterised by N_2 physisorption. Figure 2 and Table 2 compile the results of the characterisation by N_2 physisorption of the graphene aerogels, CNTs, and the two GA-CNT hybrids, containing two different amounts of CNTs. The isotherms of all materials (Figure 2a) can be considered of Type IV with hysteresis loop type H3 typical of micro-mesoporous materials. Moreover, the fact that the loop does not exhibit limiting adsorption at high P/Po is indicative of slit-shaped pores [41] with a size in the range of macropores (diameter > 50 nm) [42,43]. These macropores are evidenced in the SEM images below (Figure 3). The microporosity stems likely from the slit-shaped pores formed by the stacking of crumpled graphene nanosheets for GA and from the inner cavity of CNTs. Pore volume encompasses both

micropores and mesopores (Figure 2b and Table 2), giving rise to a bimodal pore size distribution (PSD in Figure 2b). The estimation of the micropore and mesopore surface area, S_{mic} and S_{mes} respectively, was carried out using the t-plot method. All samples are mainly mesoporous, exhibiting much larger S_{mes} than S_{mic}. CNT exhibited the largest pore volume and the largest surface area both of micro and mesopores while GA exhibits the lower values determined by N_2 physisorption. The addition of CNT in the hybrid produces an increase of the surface area with respect to GA, mainly of mesoporous surface area, leading to S_{mes} comparable or larger to that of CNTs. The PSD (Figure 2b) shows that the mean pore size of mesopores is slightly larger for GA than for CNT, i.e., 46 nm and 32 nm respectively. For the GA-CNT hybrid aerogels, the mean pore diameter is similar to that of CNTs. There is a slight increase of the mesopore surface area when the amount of CNT increases to double.
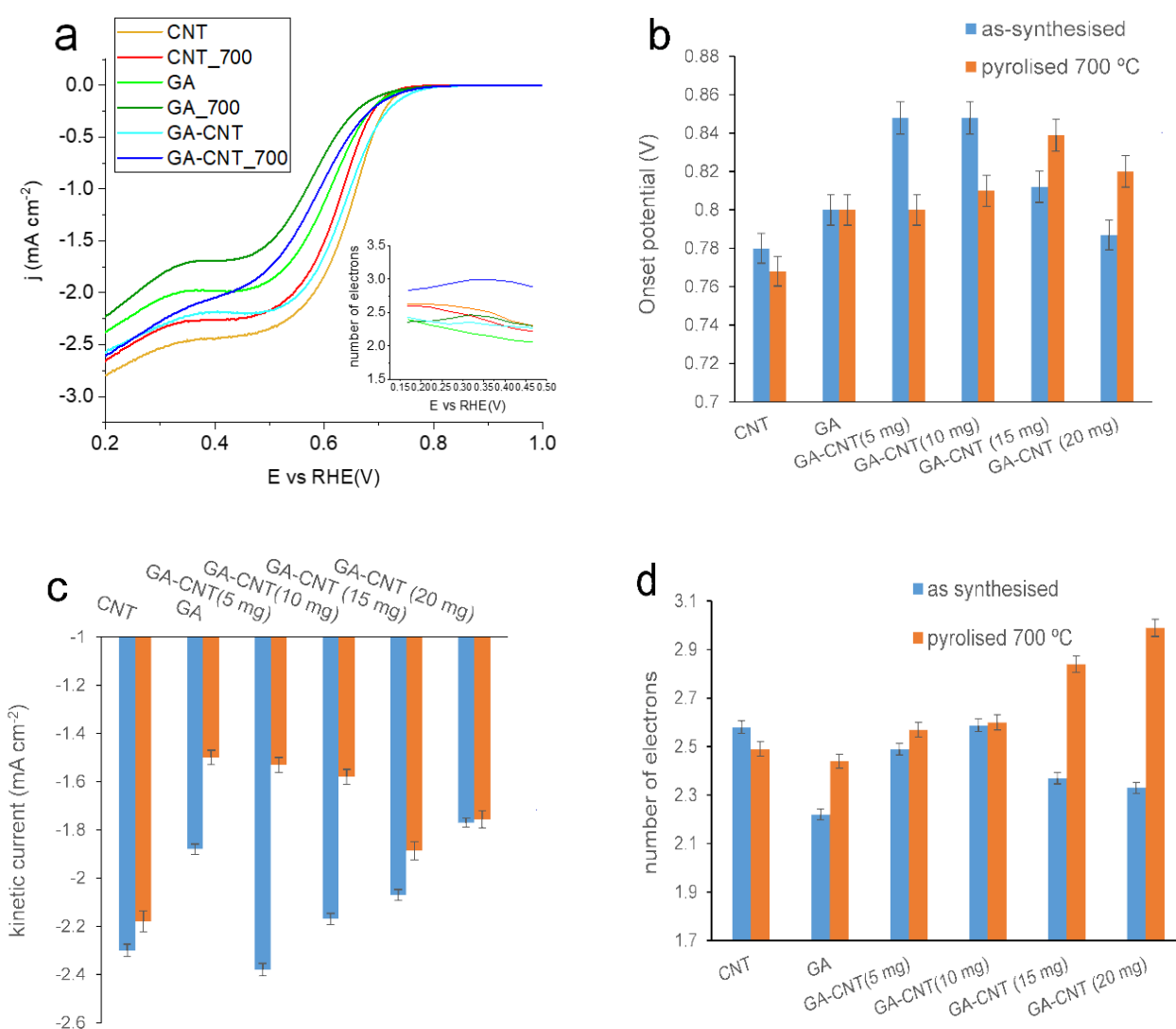
Figure 1. (**a**) LSV polarization curves and number of electrons exchanged (inset) for the CNT, GA, and the hybrid (GA-CNT) with 20 mg CNT as synthesised and after pyrolysis at 700 °C. Electrochemical parameters for different carbon materials graphene aerogel (GA), carbon nanotubes (CNT), and their hybrids with different amounts of CNT before and after pyrolysing at 700 °C. (**b**) Onset potential of LSV polarization curves in O_2 saturated 0.10 M KOH solution with a rotating rate of 1600 rpm; (**c**) kinetic current; and (**d**) number of electrons calculated from the slope of the K–L plots in a potential range of −0.3 to −0.5 V.
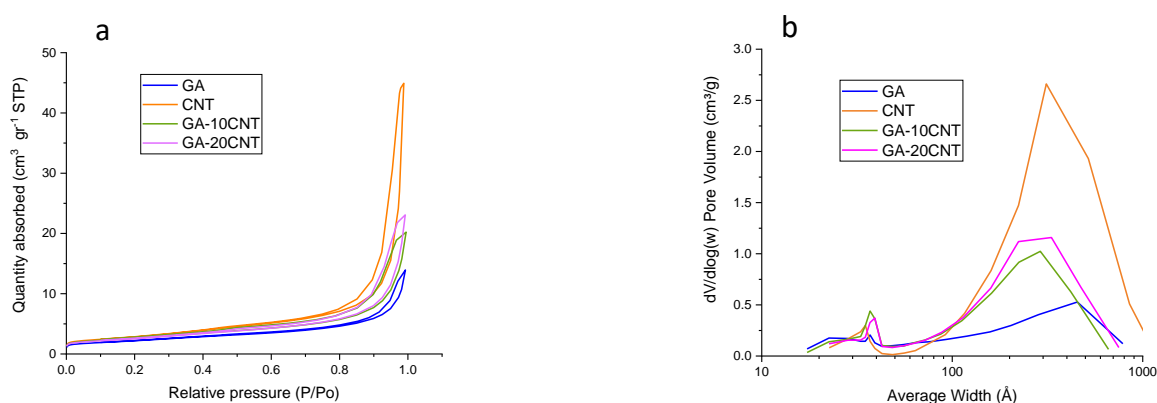
Figure 2. Characterisation by N_2 physisorption: (**a**) adsorption isotherms and (**b**) pore size distribution measured by BJH method applied to desorption isotherm.

Table 2. Textural parameters of carbon nanotubes, graphene aerogels, and hybrids thereof.

Sample	Surface Area	Pore Volume	Micropore Surface Area * (S_{mic})	External Surface Area (S_{mes})
	m^2/g	cm^3/g	m^2/g	m^2/g
CNT	228	1.55	63	165
GA	173	0.48	43	130
GA-CNT (10 mg)	208	0.7	42	165
GA-CNT (20 mg)	200	0.8	21	178

* calculated using the t-plot method to the N_2 adsorption isotherm.
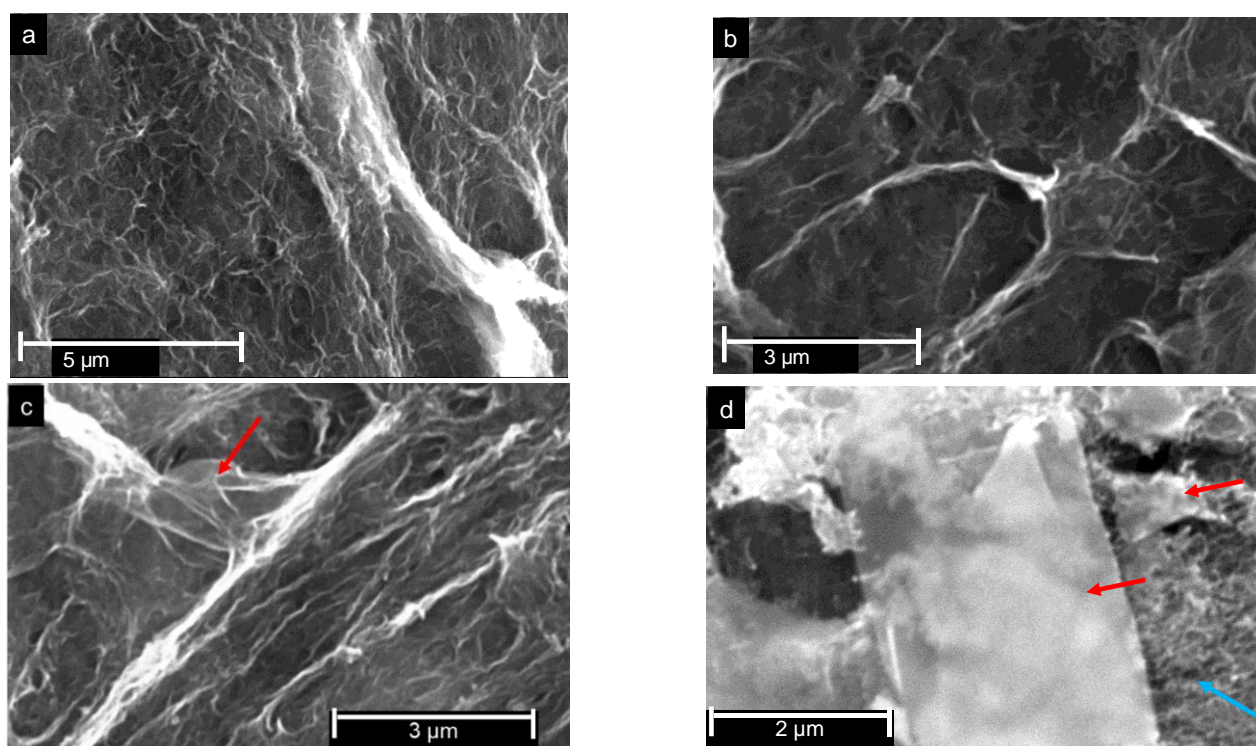
Figure 3. Representative SEM images of GA_700 (**a**,**b**) and GA-CNT(20 mg)_700 (**c**,**d**). Red arrows point to graphene sheets and blue arrow to an area of entangled CNT.

The macroscopic shape and size of GA and GA-CNT are almost comparable (Figure S3 of Supplementary Material), suggesting that the macropores of GA remain in the hybrid GA-CNT. The macropores in the hybrid are visible in SEM microscopy images (Figure 3).

GA shows the macropores formed between the ice-templated graphene sheets (Figure 3a,b). In the hybrid (Figure 3c,d), more fibrous features are observed, and some of them can be attributed to CNTs connecting the graphene sheets. However, it is difficult to distinguish between the CNTs and borders of graphene sheets at this magnification. The higher magnification image of Figure 3d shows an individual transparent graphene sheet lying on a bundle of CNTs, which are visible under the sheet and at the right-hand side. Summarising, the hierarchical porous structure of the GA-CNT hybrid combines the macroporous structure of GA and the mesoporosity of CNTs. The enhancement of the hybrid is attributed to the increase of active site exposure by macroporosity and the effect of the increased conductive paths afforded by the CNT. The macroporous structure could be beneficial for the diffusion of O_2 and electrolyte ions to the catalytic sites located on CNT and GA mesopores [33]. This may cause the enhanced onset potential and number of electrons.

The next step we explored was the introduction of an additional source of nitrogen during synthesis to dope the GA-CNT hybrid aerogels. To transform the N source into a N-C carbon bond, pyrolysis under N_2 was carried out at different temperatures, namely 500, 700, and 900 °C. As nitrogen precursors we used urea (Ur), melamine (Mel), pyrrole (Py), and ethylenediamine (EDA). For EDA and urea precursor, the linear sweep voltammetry curves (Figure S4 of Supplementary Material) hardly change as pyrolysis temperature varies. In contrast, for pyrrole and melamine, the onset potential becomes more positive and the limiting current is higher as the pyrolysis temperature increases from 500 °C to 700 °C. However, for the highest pyrolysis temperature of 900 °C, the electrochemical behaviour decays in terms of onset potential and kinetic current. Thus, the optimum pyrolysis temperature was 700 °C. It may be argued that 700 °C meets a compromise between high conductivity and high N-doping levels. Lower pyrolysis temperatures may lead to lower conductivities and higher temperatures may remove some N-atoms. Therefore, 700 °C was selected as pyrolysis temperature to compare the different nitrogen doping precursors (Figure 4).

The GA-CNT_Mel_700 exhibited higher onset potential and kinetic current than the undoped GA-CNT_700. The electrocatalytic activity of N-doped carbon materials in the oxygen reduction reaction is generally attributed to the activation of the O_2 molecule due to the enhancement of the electron-donor properties [44] and to the polarisation of the C-N bonds due to the higher electronegativity of N compared to C [45]. Nevertheless, the doping with EDA (GA-CNT_EDA_700) provided the poorest performance in terms of onset potential, kinetic current, and number of electrons, even worse than the GA-CNT_700. It is worth noting that the macroscopic shape of the aerogel synthesised in the presence of EDA (Figure S5 of Supplementary Materi) was more irregular than the other aerogels. Thus EDA affects substantially the assembling of nanosheets in the hydrogel.

Using pyrrole as N precursor provided a number of electrons closer to two and almost constant with the voltage keeping a kinetic current and onset potential in the range of the other N-doped materials. Thus, this catalyst would be an ideal candidate to synthesise H_2O_2 selectively. The microstructure of GA-CNT-Py_700 (Figure S6 Supplementary Material) shows graphene sheets very crumpled and even some graphene spheres of amorphous carbon typical from hydrothermal carbonisation of carbohydrates [46]. The number of electrons for the rest of N-doped GA-CNT electrocatalysts is close to 3, indicating a mixed mechanism between the reduction towards H_2O_2 and H_2O. Standing out among all the catalysts, the electrocatalyst doped with melamine exhibited significantly more positive onset potential and the highest kinetic current. Therefore, this is the most promising metal-free catalyst among all tested here for future optimization of a cathode in a fuel cell.

For further exploring the doping with melamine, we studied the effect of several parameters such as the amount of melamine and the type of carbon support on the electrochemical behaviour of the catalyst. Figure 5a,b compares the effect of the amount of melamine. The transition from a two stage ORR curve to a one-stage curve after the addition of melamine indicates the efficiency of the dopant in enhancing ORR process. Compared to the pristine GA-CNT_700, the addition of 150 mg of melamine provides a

significantly more positive onset potential and higher kinetic current but the improvement is only marginal for further addition of melamine (300 mg). One reason for this could be that the increase in the number of active centres by the addition of a larger amount of melamine could be counterbalanced by a decrease of electrical conductivity. The number of electrons does not vary substantially, being for all melamine-doped catalysts in the range 2.7–3 electrons (Figure 5b). The doping of the hybrid (GA-CNT) with melamine was compared with the doping of the single component supports, i.e., GA and CNT (Figure 5c,d). The N-doped GA exhibited significantly poorer performance than N-doped CNT in terms of onset potential and kinetic current. However, the hybrid GA-CNT provided a synergetic enhancement of both onset potential and kinetic current. Since the N-doping amount was similar, the enhancement may be due to the different texture of the supports as reported above. That is, the hierarchical porous structure of GA-CNT compared to only macropores for GA or micro-mesopores for CNTs.
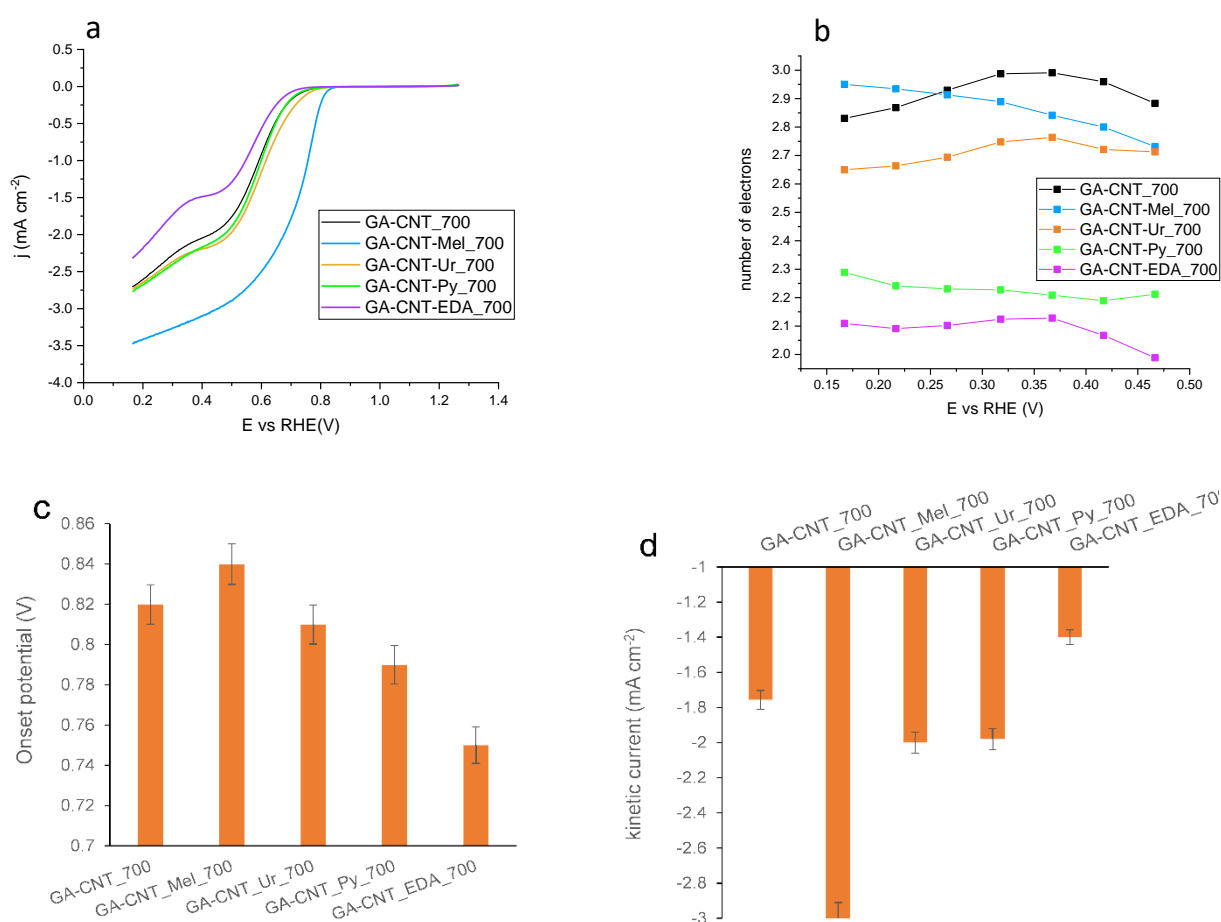
Figure 4. Effect of doping GA-CNT hybrids with different N-doping precursors pyrolysed at 700 °C: (**a**) LSV polarization curves in O_2 saturated 0.10 M KOH solution with a rotating rate of 1600 rpm; (**b**) interchanged number of electrons; (**c**) onset potentials; (**d**) and kinetic currents.

As seen heretofore, the doping of the GA-CNT hybrid with melamine enhanced substantially the kinetic current and onset potential with respect to pristine carbon materials. However, the number of electrons does not go beyond three, the same value as that found also for pristine GA-CNT_700, suggesting that melamine doping partially reduces O_2 to H_2O_2. A strategy commonly used to push the mechanism towards four electrons is the addition of metal nanoparticles [47]. Here, we added to the CNT-GA hybrid a transition metal (Fe) and N containing compound (phenanthroline), which form a metal complex [48–50]. The results for the GA-CNT doped with Fe (GA-CNT-FeN) pyrolysed at different temperatures (500–800 °C) and also a commercial 20%Pt/vulcanXC-72 are shown in Figure 6,

Figures S7–S11, and Table S1. The onset potential of the metal-doped GA-CNT-FeN is more positive than for the melamine doped catalysts tested previously and the number of electrons is closer to four. Among the different pyrolysis temperatures, 700 °C leads to the highest kinetic current and most positive onset potential (Figure 6c). The number of electrons and Tafel slope are similar to those of the commercial 20% Pt/vulcanXC-72 suggesting that both follow predominantly one-step four-electron reduction pathway (Figure 6d). In many cases, a variety of Tafel slopes are reported, and most are potential-dependent. For instance, it is reported [51] that in an alkaline solution of 1 M NaOH, Pt/C exhibits a two-step Tafel slope of 65–82 mV dec^{-1} that increases to >100 mV dec^{-1} with increasing overpotential. Tafel slope dependence on each coverage is considered to determine the rate-determined step. Tafel slope of 79 mV/dec for the Pt/C catalyst, similar to our results with 20% Pt/VulcanXC72 (86 mV/dec), are attributed to the first electron transfer as rate-determining step [52,53]. The GA-CNT_FeN_700 have a Tafel slope of 67 mV/dec which is lower than for Pt/C, suggesting a slight change in the reaction mechanism but far from the higher Tafel slopes (120 mV/dec) attributed to a change in the rate-determining step as, for example, the O$_2$ adsorption step. The increase of pyrolysis temperature to 800 °C degrades the number of electrons and kinetic current as observed for the N-doped catalyst. Thus, this high temperature probably removes C-FeNx-C active sites.
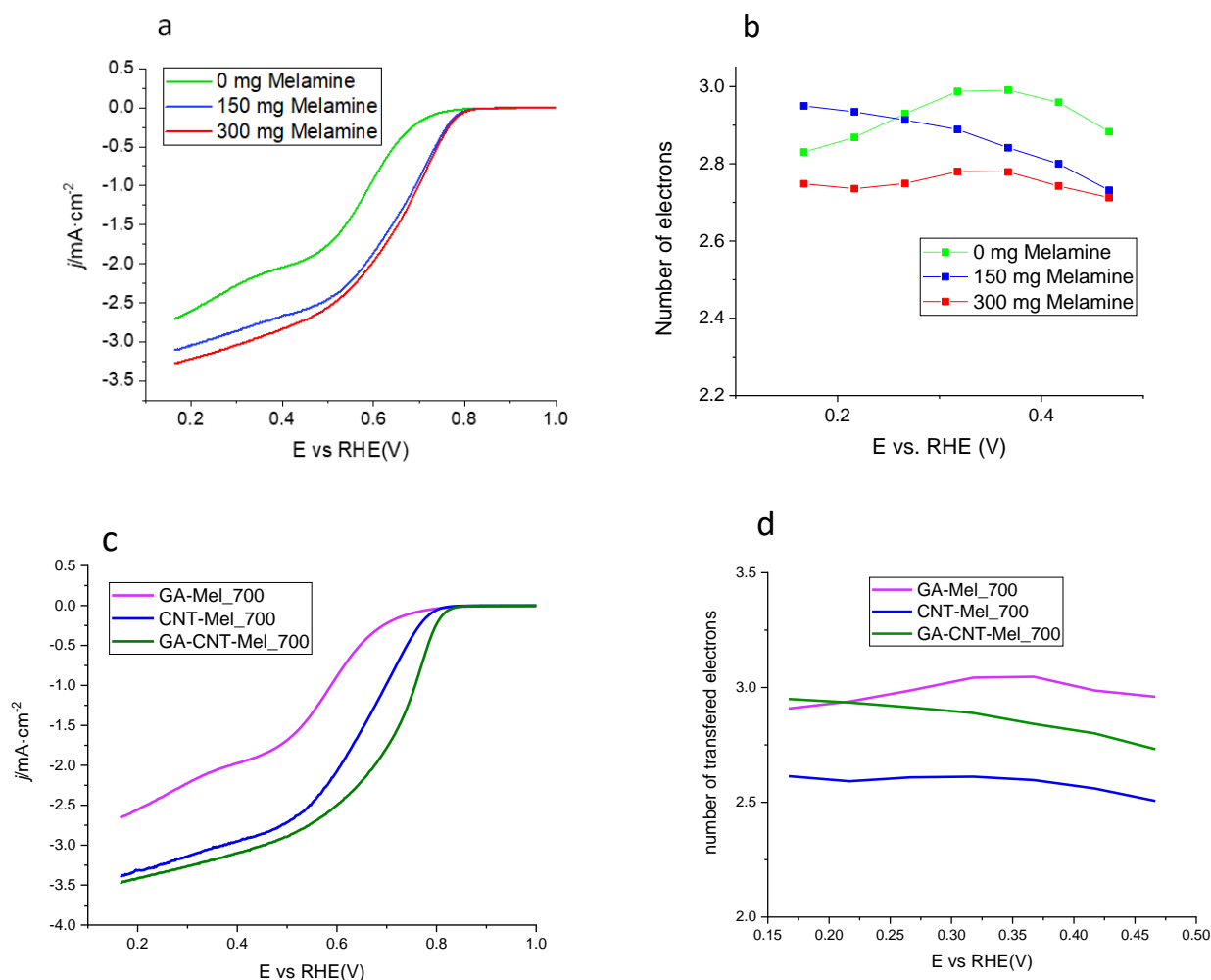
Figure 5. Effect of N-doping using melamine as precursor: (**a**) polarization curves for different amounts of melamine in O$_2$ saturated 0.10 M KOH solution with a rotating rate of 1600 rpm; (**b**) number of electrons for polarization curves in (**a**); (**c**) polarization curves for N-doping using melamine for graphene aerogel, carbon nanotubes and hybrids thereof; (**d**) and number of electrons transferred for the different supports in (**c**).
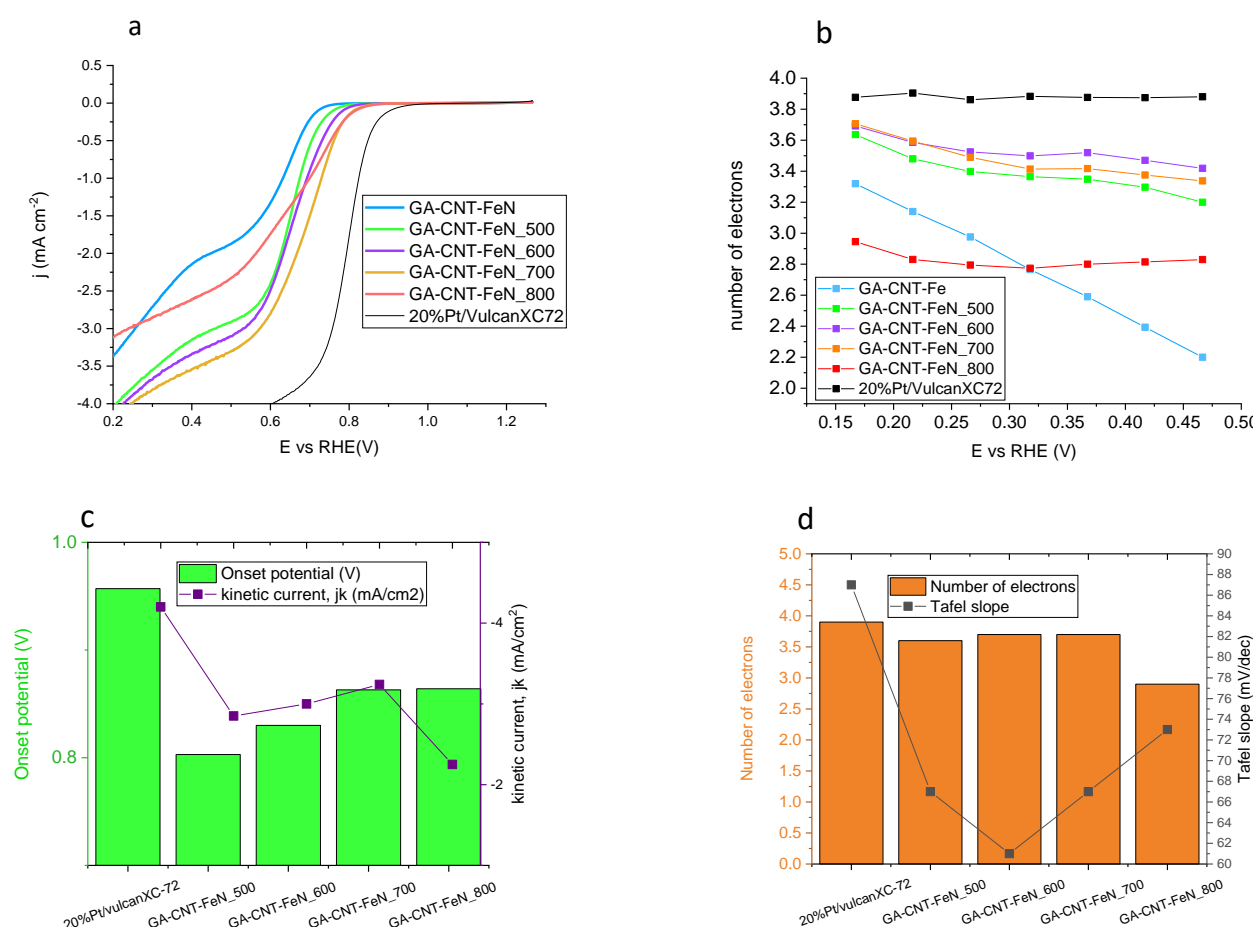
Figure 6. Polarization curves in O_2 saturated 0.10 M KOH solution with a rotating rate of 1600 rpm. (**a**) Number of electrons (**b**) and other parameters derived from the treatment of polarization curves (**c,d**) for Fe-containing GA-CNT pyrolysed at different temperatures and a commercial 20% Pt/VulcanXC72.

Although the Fe nominal loading in the hydrothermal solution was 3 wt%, part of the Fe remains in the solution as observed by the brownish colour of liquid after hydrothermal synthesis (Figure S12), suggesting that not all Fe phenanthroline on the mother liquid was incorporated in the aerogel. In fact, ICP revealed that the Fe loading on the GA-CNT-FeN_700 and GA-CNT-FeN_800 was 1.0 wt% (=0.22 at%) and 1.1 wt% (=0.24 at%), respectively. The Fe atom percentage determined by XPS is shown in Figure 7 and it is 0.12 at% and 0.10 at% for GA-CNT-FeN_700 and GA-CNT-FeN_800, respectively. The percentage of Fe determined by XPS is somehow lower that that determined by elemental analysis. Moreover, it decreases as temperature increases which may be attributed to the formation of larger nanoparticles by effect of temperature. XRD analysis did not show any diffraction corresponding to Fe (Figure S13) suggesting that Fe is dispersed to very small particles size which is not detected by XRD.

The Fe containing catalyst was further characterised by XPS (Figure S14). The 2p photoelectron peaks appear around 711.2 and 724.0 eV, which are characteristic of Fe^{3+} in Fe_2O_3 [54] or to Fe-Nx species [55]. No component related to zero-valent Fe was observed. We also performed fitting of the N 1s spectra (Figure 8). The common five peaks for N1s were pyridinic N with binding energy of 398.2 eV, N in FeNx with B.E = 399.7 eV, pyrrolic N (or hydrogenated pyridinic) with B.E = 401.0 eV, graphitic N with B.E = 402.1 eV, and N-oxide with B.E at 403.6 eV [55,56]. The relative contribution of FeNx at 399.7 eV remains almost constant for all treatment temperatures (Figure 8b) indicating that these species are stable up to 800 °C. FeNx species are claimed as the active phase for the 4-electron O_2 reduction pathway [57]. The relative contribution of the rest of N species changes with

the treatment temperature. From 600 °C upwards, the relative contribution of pyridinic decreases significantly and these groups are probably transformed in pyrrolic groups, whose relative contribution increases as treatment temperature rises.
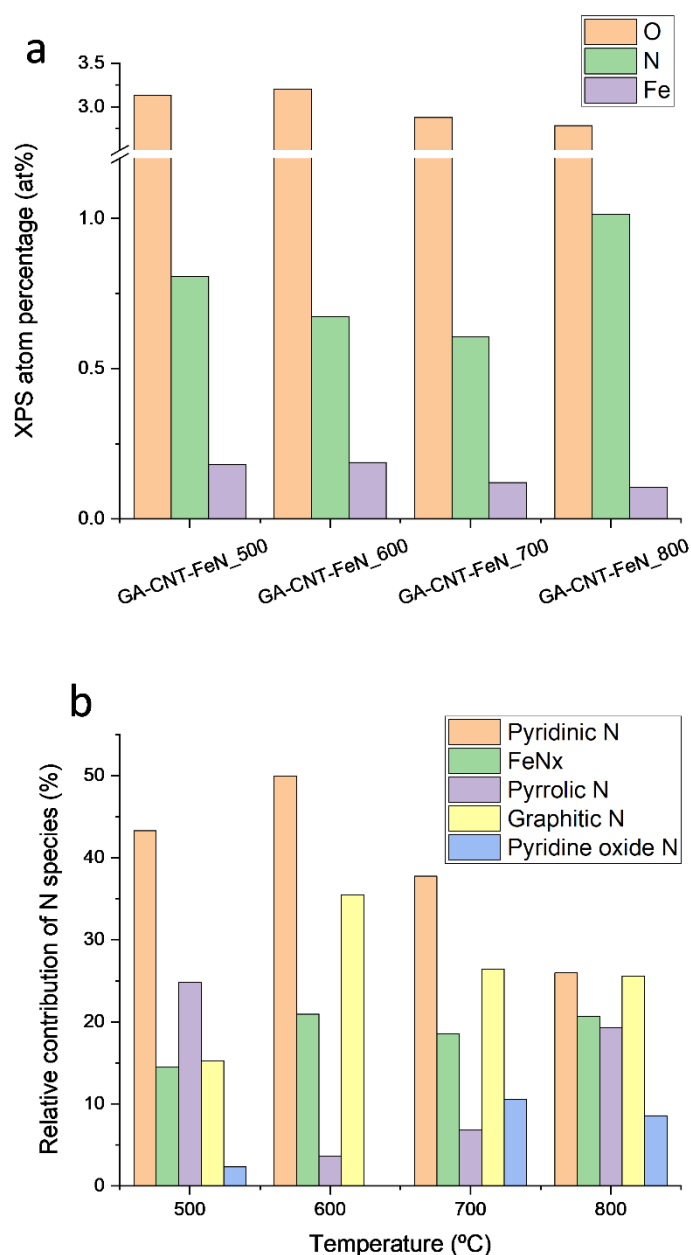

Figure 7. XPS quantification: (**a**) atomic percentages determined by XPS and (**b**) relative contribution of N species determined by N 1s XPS deconvolution.

The electrocatalyst GA-CNT-FeN_700 was characterised further by STEM-HAADF. By this technique, the Fe metal can be distinguished in the images by the lightest contrast. At low magnification, no nanoparticles were observed (Figure 9a). At higher magnifications, no metal nanoparticles larger than 1 nm were detected in most of the images (Figure 9b), suggesting that all the Fe was highly dispersed as FeNx or small subnanometric Fe oxide clusters.
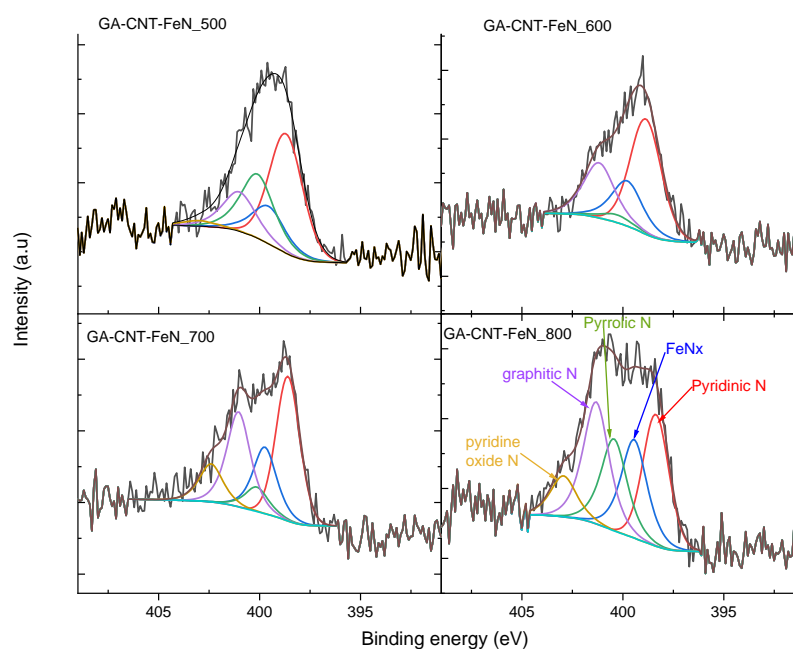
Figure 8. Deconvolution of the N1s XPS core level spectra.
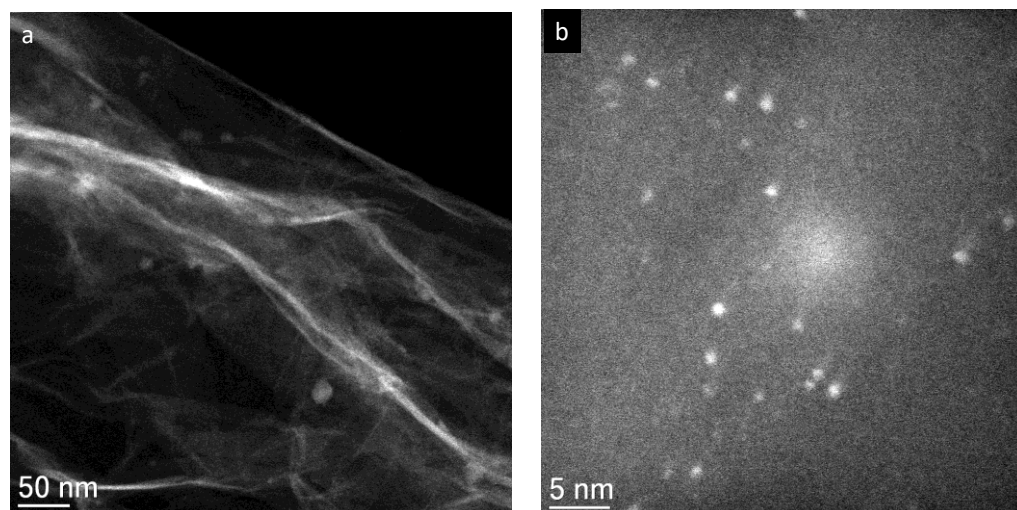
Figure 9. Representative STEM-HAADF images of catalyst GA-CNT-FeN_700 at two different magnifications: (**a**) low magnification STEM image; (**b**) high-magnification image. The lightest contrast corresponds to Fe oxide clusters or FeMx.

3. Materials and Methods

3.1. Aerogel Preparation and N-Doping

Figure S15 of Supplementary Material illustrates the methods used for the preparation of the different materials. Graphene aerogel (GA) was prepared by the hydrothermal reduction/gelation of graphene oxide (GO) [32,58]. In brief, 8 mL of 4 mg/mL GO dispersion (supplied by Graphenea Co., San Sebastián, Spain, ref GO-4-1000) were diluted with 8 mL distilled water in a glass vial and this vial was introduced in a Teflon-lined autoclave as that shown in Figure S1. The autoclave was introduced in an oven at 185 °C, reaching an autogenous pressure and kept for 20 h. Subsequently, the autoclave was withdrawn from the oven and left to cool down at ambient conditions during 2 h. After this, a cylindrical rGO monolithic hydrogel had been segregated inside the vial, which was subsequently immersed in liquid nitrogen (−196 °C) for 10 min and then freeze-dried in lyophiliser (Telstar Cryodos) under 0.3 mbar and 223 K for 48 h to obtain the graphene aerogel (GA).

For the preparation of the hybrid graphene aerogel with carbon nanotubes (GA-CNT), 20 mg of CNT (Nanocyl 7000 previously oxidized with 65% HNO_3 at room temperature for 4 h) was added to the GO dispersion and tip sonicated for 5 min. Subsequently, the same process described previously to synthesised GA was applied.

N-doped GA-CNT hybrids were obtained in one-pot using three different N-precursor, urea (Ur), ethylenediamine (EDA), and pyrrole (Py). The one-pot method consisted of well dispersing an adequate amount of the N-precursor into the GO+CNT aqueous dispersion to have a final nitrogen concentration of 7 wt% with respect to the final GA-CNT weight. For doping the GA-CNT with Fe-nitrogen, the amount of Fe acetate corresponding to a 3 wt% Fe with respect to GA-CNT was dissolved in absolute ethanol (8 mL). Afterwards, 1,10-phenanthroline (2.0 equiv., Aldrich $\geq$ 99%) was added and the resulting solution was stirred for 1 h at 60 °C. Subsequently, the Fe acetate solution was mixed with 8 mL GO and CNT and the hydrothermal treatment was carried out as described previously.

As melamine was not soluble in water, the doping with melamine was performed ex situ, starting from the previously formed CNT-GA hybrid. For N-doping with melamine, the amount corresponding to a 7% nitrogen was mixed with the GA-CNT hybrid mechanically in solid phase using an agate mortar.

All the aerogels obtained as above were subsequently pyrolysed in N_2 at different temperatures, namely 500 °C, 700 °C, and 900 °C.

3.2. Electrochemical Characterisation

Cyclic voltammetry (CV) and rotating disk electrode (RDE) studies were conducted using Autolab PGSTAT30 potentiostat equipped with an analogue linear sweep generator at the sweep rate of 10 mV s^{-1}. A glass cell with 0.1 M KOH as electrolyte, Ag/AgCl as reference electrode, and Pt wire as the counter electrode were used. The potentials are referred to the reversible hydrogen electrode (RHE)

The catalyst ink was prepared by mixing 10.0 mg of the catalyst sample, 5 mL iso-propanol, and 50 µL Nafion solution (5 wt%) and sonicated for half an hour. The working rotating ring disk (RDE) electrode (Pine instruments) was prepared by drop casting 52.5 µL of catalyst ink onto a pretreated glassy carbon (GC) electrode (5.5 mm diameter and 0.2376 cm geometric area) and then dried at room temperature. The catalyst density resulted in 445 µg cm^{-2}. As a benchmark, a 20 wt% Pt on Vulcan XC72R (Sigma-Aldrich, St. Louis, MO, USA) catalyst was used. All aqueous solutions were prepared using ultra-pure water (18 MΩ cm, <3 ppb TOC) and supra-pure KOH (Sigma–Aldrich, St. Louis, MO, USA). In O_2-reduction experiments, a saturation level of O_2 was maintained by constantly bubbling O_2.

The apparent number of electrons transferred per O_2 molecule was calculated using the first-order Koutecky–Levich equation [59]:

$$\frac{1}{J} = \frac{1}{J_k} + \frac{1}{J_d} \tag{3}$$

where J_k is the kinetic current density and J_d is the diffusion-limited current density through the expression $J_d = B\,\omega^{\frac{1}{2}} = 0.62\,n\,F\,\gamma^{-1/6}D_{O_2}^{2/3}C_{O_2}\omega^{\frac{1}{2}}$. Here, F is the Faraday constant, n is the number of electrons, γ is the kinematic viscosity of the electrolyte, C_{O_2} is the bulk oxygen concentration in the electrolyte (1.15×10^{-6} mol cm^{-3}), D_{O_2} is the oxygen diffusion coefficient (1.95×10^{-5} cm^2 s^{-1}) [60], and ω is the angular velocity of the electrode. The kinetic current density (J_k) and the Koutecky–Levich slope ($1/B$) can be obtained from a plot of $1/J$ vs. $\omega^{-1/2}$.

3.3. Electrocatalyst Characterisation

Physisorption of N_2 at 77 K was carried out in a Micromeritics ASAP 2020 apparatus (Micromeritics Corporate, Norcross, GA, USA) after outgassing the sample for 4 h at 423 K. The surface area (S_{N2}) has been calculated by applying the BET (Brunauer, Emmet, and Teller) theory to the adsorption isotherm in the relative pressure range 0.01–0.10 following

standard ASTM-4365. Pore volume was calculated from the amount of N_2 adsorbed at a relative pressure of 0.99. Pore-size distribution was obtained applying the BJH method (Barrett-Joyner-Halenda) to the adsorption branch of the N_2 isotherm using the DataMaster V4.0 software and assuming slit pore geometry. The model fitted quite well to the isotherm with a standard deviation of ~0.05 cm^3 g^{-1} STP. The micropore surface area (S_{mic}) was calculated by the t-plot method and the external surface area (S_{mes}) by subtraction from the total surface area.

SEM analysis was carried out with a microscope SEM EDX Hitachi S-3400 N with variable pressure up to 270 Pa and with an analyser EDX Röntec XFlash de Si(Li). The images were obtained both from the secondary and backscattered signal.

The X-ray photoelectron spectroscopy (XPS) was carried out with an ESCAPlus Omnicrom equipped with a Mg Kα radiation source to excite the sample. All measurements were performed under UHV, better than 10^{-10} Torr. Calibration of the instrument was performed with Ag 3 d$_{5/2}$ line at 368.27 eV. The curve fitting of the spectra was performed using CASA XPS software. For the correction of the binding energies of the spectra, the C 1s signal at 284.6 eV was used as reference. The XPS peaks were fitted to GL(70) lineshape (a combination of 30% Gaussian and 70% Lorentzian character), performing a Shirley background subtraction. In the fitting procedure the FWHM (full width at half maximum) values were fixed at a maximum limit of 2 eV.

Scanning transmission electron microscopy in high-angle annular dark field mode (STEM-HAADF) was carried using a FEI TECNAI F30 electron microscope equipped with Gatan energy filter and cold field-emission gun (FEG) operated at 300 kV with a 1.5 Å lattice resolution. TEM specimens were prepared by ultrasonic dispersion in ethanol of powder catalyst. A drop of the suspension was applied to a holey carbon support grid.

X-ray diffraction (XRD) patterns were recorded using a Bruker D8 Advance diffractometer in configuration theta-theta using nickel-filtered CuK α radiation (wave length = 1.54 Å), a graphite monochromatic source and scintillation detector. Then, 2θ angles from 3 to 80° were scanned with a length step of 0.05 and an accumulation time of 3 s. ICP-OES (Inductive coupled plasma-optical emission spectroscopy) was performed using a Spectroblue de Ametek apparatus.

4. Conclusions

Pure carbon materials such as CNT and GA exhibited modest activity in ORR and the number of electrons involved was between 2 and 2.5. The formation of a hybrid of CNT and GA affords a synergetic enhancement of the performance that depends on the amount of CNTs and on a thermal post-treatment. A thermal post-treatment enhanced the performance of GA-CNT hybrids with the higher amount of CNTs while it was the reverse for the lower amount of CNTs. Thus, the GA-CNT hybrid with a higher amount of CNT (20 mg) and pyrolysed at 700 °C provided the best performance and the highest number of electrons (around 3) among the undoped carbon materials. The doping of the GA-CNT hybrid with nitrogen, using melamine as a nitrogen source, improved significantly the performance of the catalyst in terms of onset potential and kinetic current but did not provide a number of electrons higher than three. The enhanced performance of the hybrid with respect to the pure components can be ascribed to its hierarchical porous structure encompassing the macroporosity of GA and the mesoporosity of CNTs. Likewise, the GA-CNT hybrid exhibited surface area of mesopores comparable or larger than that of the single components. The macroporous structure may affect advantageously the diffusion of the electrolyte and O_2, increasing active site exposure while CNT increases the electrically conductive paths between rGO sheets of GA. The electrocatalyst prepared by adding Fe and phenanthroline during the preparation of GA-CNT hybrid provided almost complete selectivity to H_2O, more positive onset potential, and higher kinetic current than the metal-free catalyst, the behaviour approaching that of benchmark Pt electrocatalyst. The enhancement of ORR performance is attributed to the presence of FeNx sites. Therefore, the CNT-graphene aerogel hybrid has excellent prospects to be used as self-standing structured

cathode in fuel cells due to its porous texture favourable for ions and O_2 diffusion. One of the challenges for future catalyst improvements would be to attain a high density of single metal sites.

References

1. Yang, L.; Shui, J.; Du, L.; Shao, Y.; Liu, J.; Dai, L.; Hu, Z. Carbon-Based Metal-Free ORR Electrocatalysts for Fuel Cells: Past, Present, and Future. *Adv. Mater.* **2019**, *31*, e1804799. [CrossRef]
2. Wang, D.-W.; Su, D. Heterogeneous nanocarbon materials for oxygen reduction reaction. *Energy Environ. Sci.* **2013**, *7*, 576–591. [CrossRef]
3. Inaba, M.; Yamada, H.; Tokunaga, J.; Matsuzawa, K.; Hatanaka, A.; Tasaka, A. Hydrogen Peroxide Formation as a Degradation Factor of Polymer Electrolyte Fuel Cells. *ECS Trans.* **2006**, *1*, 315–322. [CrossRef]
4. Siahrostami, S.; Villegas, S.J.; Mostaghimi, A.H.B.; Back, S.; Farimani, A.B.; Wang, H.; Persson, K.A.; Montoya, J. A Review on Challenges and Successes in Atomic-Scale Design of Catalysts for Electrochemical Synthesis of Hydrogen Peroxide. *ACS Catal.* **2020**, *10*, 7495–7511. [CrossRef]
5. Jiang, Y.; Ni, P.; Chen, C.; Lu, Y.; Yang, P.; Kong, B.; Fisher, A.; Wang, X. Selective Electrochemical H_2O_2 Production through Two-Electron Oxygen Electrochemistry. *Adv. Energy Mater.* **2018**, *8*, 1801909. [CrossRef]
6. Siahrostami, S.; Verdaguer-Casadevall, A.; Karamad, M.; Deiana, D.; Malacrida, P.; Wickman, B.; Escudero-Escribano, M.; Paoli, E.A.; Frydendal, R.; Hansen, T.W.; et al. Enabling direct H_2O_2 production through rational electrocatalyst design. *Nat. Mater.* **2013**, *12*, 1137–1143. [CrossRef] [PubMed]
7. Jirkovský, J.S.; Panas, I.; Ahlberg, E.; Halasa, M.; Romani, S.; Schiffrin, D.J. Single Atom Hot-Spots at Au–Pd Nanoalloys for Electrocatalytic H_2O_2 Production. *J. Am. Chem. Soc.* **2011**, *133*, 19432–19441. [CrossRef]
8. Ba, H.; Liu, Y.; Truong-Phuoc, L.; Duong-Viet, C.; Nhut, J.-M.; Nguyen, D.L.; Ersen, O.; Tuci, G.; Giambastiani, G.; Pham-Huu, C. N-Doped Food-Grade-Derived 3D Mesoporous Foams as Metal-Free Systems for Catalysis. *ACS Catal.* **2016**, *6*, 1408–1419. [CrossRef]
9. Trogadas, P.; Fuller, T.F.; Strasser, P. Carbon as catalyst and support for electrochemical energy conversion. *Carbon* **2014**, *75*, 5–42. [CrossRef]
10. Qu, L.; Liu, Y.; Baek, J.-B.; Dai, L. Nitrogen-Doped Graphene as Efficient Metal-Free Electrocatalyst for Oxygen Reduction in Fuel Cells. *ACS Nano* **2010**, *4*, 1321–1326. [CrossRef]

11. Lin, Z.; Waller, G.; Liu, Y.; Liu, M.; Wong, C.-P. Facile Synthesis of Nitrogen-Doped Graphene via Pyrolysis of Graphene Oxide and Urea, and its Electrocatalytic Activity toward the Oxygen-Reduction Reaction. *Adv. Energy Mater.* **2012**, *2*, 884–888. [CrossRef]

12. Cui, Z.; Wang, S.; Zhang, Y.; Cao, M. A simple and green pathway toward nitrogen and sulfur dual doped hierarchically porous carbons from ionic liquids for oxygen reduction. *J. Power Sources* **2014**, *259*, 138–144. [CrossRef]

13. She, Y.; Lu, Z.-G.; Ni, M.; Li, L.; Leung, M.K. Facile Synthesis of Nitrogen and Sulfur Codoped Carbon from Ionic Liquid as Metal-Free Catalyst for Oxygen Reduction Reaction. *ACS Appl. Mater. Interfaces* **2015**, *7*, 7214–7221. [CrossRef] [PubMed]

14. Sun, Y.; Sinev, I.; Ju, W.; Bergmann, A.; Dresp, S.; Kühl, S.; Spoeri, C.; Schmies, H.; Wang, H.; Bernsmeier, D.; et al. Efficient Electrochemical Hydrogen Peroxide Production from Molecular Oxygen on Nitrogen-Doped Mesoporous Carbon Catalysts. *ACS Catal.* **2018**, *8*, 2844–2856. [CrossRef]

15. Fellinger, T.-P.; Hasché, F.; Strasser, P.; Antonietti, M. Mesoporous Nitrogen-Doped Carbon for the Electrocatalytic Synthesis of Hydrogen Peroxide. *J. Am. Chem. Soc.* **2012**, *134*, 4072–4075. [CrossRef]

16. Iglesias, D.; Giuliani, A.; Melchionna, M.; Marchesan, S.; Criado, A.; Nasi, L.; Bevilacqua, M.; Tavagnacco, C.; Vizza, F.; Prato, M.; et al. N-Doped Graphitized Carbon Nanohorns as a Forefront Electrocatalyst in Highly Selective O_2 Reduction to H_2O_2. *Chem* **2018**, *4*, 106–123. [CrossRef]

17. Perazzolo, V.; Durante, C.; Pilot, R.; Paduano, A.; Zheng, J.; Rizzi, G.A.; Martucci, A.; Granozzi, G.; Gennaro, A. Nitrogen and sulfur doped mesoporous carbon as metal-free electrocatalysts for the in situ production of hydrogen peroxide. *Carbon* **2015**, *95*, 949–963. [CrossRef]

18. Lee, Y.-H.; Li, F.; Chang, K.-H.; Hu, C.-C.; Ohsaka, T. Novel synthesis of N-doped porous carbons from collagen for electrocatalytic production of H_2O_2. *Appl. Catal. B Environ.* **2012**, *126*, 208–214. [CrossRef]

19. Zhang, D.; Liu, T.; Yin, K.; Liu, C.; Wei, Y. Selective H2O2 production on N-doped porous carbon from direct carbonization of metal organic frameworks for electro-Fenton mineralization of antibiotics. *Chem. Eng. J.* **2019**, *383*, 123184. [CrossRef]

20. Yan, X.; Jia, Y.; Odedairo, T.; Zhao, X.; Jin, Z.; Zhu, Z.; Yao, X. Activated carbon becomes active for oxygen reduction and hydrogen evolution reactions. *Chem. Commun.* **2016**, *52*, 8156–8159. [CrossRef]

21. Oh, J.; Park, S.; Jang, D.; Shin, Y.; Lim, D.; Park, S. Metal-free N-doped carbon blacks as excellent electrocatalysts for oxygen reduction reactions. *Carbon* **2019**, *145*, 481–487. [CrossRef]

22. Kim, H.W.; Ross, M.B.; Kornienko, N.; Zhang, L.; Guo, J.; Yang, P.; McCloskey, B.D. Efficient hydrogen peroxide generation using reduced graphene oxide-based oxygen reduction electrocatalysts. *Nat. Catal.* **2018**, *1*, 282–290. [CrossRef]

23. Shao, Y.; Yin, G.; Zhang, J.; Gao, Y. Comparative investigation of the resistance to electrochemical oxidation of carbon black and carbon nanotubes in aqueous sulfuric acid solution. *Electrochim. Acta* **2006**, *51*, 5853–5857. [CrossRef]

24. You, P.; Kamarudin, S. Recent progress of carbonaceous materials in fuel cell applications: An overview. *Chem. Eng. J.* **2017**, *309*, 489–502. [CrossRef]

25. Ferrero, G.A.; Preuss, K.; Fuertes, A.B.; Sevilla, M.; Titirici, M.-M. The influence of pore size distribution on the oxygen reduction reaction performance in nitrogen doped carbon microspheres. *J. Mater. Chem. A* **2016**, *4*, 2581–2589. [CrossRef]

26. Wang, J.; Kong, H.; Zhang, J.; Hao, Y.; Shao, Z.; Ciucci, F. Carbon-based electrocatalysts for sustainable energy applications. *Prog. Mater. Sci.* **2020**, *116*, 100717. [CrossRef]

27. Bi, H.; Yin, K.; Xie, X.; Zhou, Y.; Wan, N.; Xu, F.; Banhart, F.; Sun, L.; Ruoff, R.S. Low Temperature Casting of Graphene with High Compressive Strength. *Adv. Mater.* **2012**, *24*, 5124–5129. [CrossRef]

28. Garcia-Bordejé, E.; Benito, A.; Maser, W. Graphene aerogels via hydrothermal gelation of graphene oxide colloids: Fine-tuning of its porous and chemical properties and catalytic applications. *Adv. Colloid Interface Sci.* **2021**, *292*, 102420. [CrossRef]

29. Wang, Y.; Wu, Y.; Huang, Y.; Zhang, F.; Yang, X.; Ma, Y.; Chen, Y. Preventing Graphene Sheets from Restacking for High-Capacitance Performance. *J. Phys. Chem. C* **2011**, *115*, 23192–23197. [CrossRef]

30. Liao, Y.; Mustonen, K.; Tulić, S.; Skákalová, V.; Khan, S.A.; Laiho, P.; Zhang, Q.; Li, C.; Monazam, M.R.A.; Kotakoski, J.; et al. Enhanced Tunneling in a Hybrid of Single-Walled Carbon Nanotubes and Graphene. *ACS Nano* **2019**, *13*, 11522–11529. [CrossRef]

31. Dong, X.; Li, B.; Wei, A.; Cao, X.; Chan-Park, M.; Zhang, H.; Li, L.-J.; Huang, W.; Chen, P. One-step growth of graphene–carbon nanotube hybrid materials by chemical vapor deposition. *Carbon* **2011**, *49*, 2944–2949. [CrossRef]

32. García-Bordejé, E.; Víctor-Román, S.; Sanahuja-Parejo, O.; Benito, A.M.; Maser, W.K. Control of the microstructure and surface chemistry of graphene aerogels via pH and time manipulation by a hydrothermal method. *Nanoscale* **2018**, *10*, 3526–3539. [CrossRef]

33. Rodríguez-Mata, V.; Hernández-Ferrer, J.; Carrera, C.; Benito, A.M.; Maser, W.K.; García-Bordejé, E. Towards high-efficient microsupercapacitors based on reduced graphene oxide with optimized reduction degree. *Energy Storage Mater.* **2020**, *25*, 740–749. [CrossRef]

34. Chen, P.; Xiao, T.-Y.; Qian, Y.-H.; Li, S.-S.; Yu, S.-H. A Nitrogen-Doped Graphene/Carbon Nanotube Nanocomposite with Synergistically Enhanced Electrochemical Activity. *Adv. Mater.* **2013**, *25*, 3192–3196. [CrossRef]

35. Cheng, Y.; Zhang, J.; Jiang, S.P. Are metal-free pristine carbon nanotubes electrocatalytically active? *Chem. Commun.* **2015**, *51*, 13764–13767. [CrossRef]

36. Yan, D.; Li, Y.; Huo, J.; Chen, R.; Dai, L.; Wang, S. Defect Chemistry of Nonprecious-Metal Electrocatalysts for Oxygen Reactions. *Adv. Mater.* **2017**, *29*, 1606459. [CrossRef]

37. Jiang, S.; Li, Z.; Wang, H.; Wang, Y.; Meng, L.; Song, S. Tuning nondoped carbon nanotubes to an efficient metal-free electrocatalyst for oxygen reduction reaction by localizing the orbital of the nanotubes with topological defects. *Nanoscale* **2014**, *6*, 14262–14269. [CrossRef] [PubMed]
38. Jia, Y.; Zhang, L.; Du, A.; Gao, G.; Chen, J.; Yan, X.; Brown, C.L.; Yao, X. Defect Graphene as a Trifunctional Catalyst for Electrochemical Reactions. *Adv. Mater.* **2016**, *28*, 9532–9538. [CrossRef] [PubMed]
39. Rocha, I.M.; Soares, O.S.G.P.; Figueiredo, J.L.; Freire, C.; Pereira, M.F.R. Bifunctionality of the pyrone functional group in oxidized carbon nanotubes towards oxygen reduction reaction. *Catal. Sci. Technol.* **2017**, *7*, 1868–1879. [CrossRef]
40. Seredych, M.; Szczurek, A.; Fierro, V.; Celzard, A.; Bandosz, T.J. Electrochemical Reduction of Oxygen on Hydrophobic Ultramicroporous PolyHIPE Carbon. *ACS Catal.* **2016**, *6*, 5618–5628. [CrossRef]
41. Kaneko, K. Determination of pore size and pore size distribution: 1. Adsorbents and catalysts. *J. Membr. Sci.* **1994**, *96*, 59–89. [CrossRef]
42. Balbuena, P.B.; Gubbins, K.E. Classification of adsorption behavior: Simple fluids in pores of slit-shaped geometry. *Fluid Phase Equilibria* **1992**, *76*, 21–35. [CrossRef]
43. Sing, K.S.W.; Everett, D.H.; Haul, R.A.W.; Moscou, L.; Pierotti, R.A.; Rouquerol, J.; Siemieniewska, T. Reporting Physisorption Data for Gas/Solid Systems. In *Handbook of Heterogenous Catalysis*; Wiley: Hoboken, NJ, USA, 2008; pp. 1217–1230. [CrossRef]
44. Liu, H.; Liu, Y.; Zhu, D. Chemical doping of graphene. *J. Mater. Chem.* **2010**, *21*, 3335–3345. [CrossRef]
45. Okamoto, Y. First-principles molecular dynamics simulation of O_2 reduction on nitrogen-doped carbon. *Appl. Surf. Sci.* **2009**, *256*, 335–341. [CrossRef]
46. Roldán, L.; Truong-Phuoc, L.; Ansón-Casaos, A.; Pham-Huu, C.; García-Bordejé, E. Mesoporous carbon doped with N,S heteroatoms prepared by one-pot auto-assembly of molecular precursor for electrocatalytic hydrogen peroxide synthesis. *Catal. Today* **2018**, *301*, 2–10. [CrossRef]
47. Wang, J.; Kim, J.; Choi, S.; Wang, H.; Lim, J. A Review of Carbon-Supported Nonprecious Metals as Energy-Related Electrocatalysts. *Small Methods* **2020**, *4*, 2000621. [CrossRef]
48. Jagadeesh, R.V.; Surkus, A.-E.; Junge, H.; Pohl, M.-M.; Radnik, J.; Rabeah, J.; Huan, H.; Schünemann, V.; Brückner, A.; Beller, M. Nanoscale Fe_2O_3-Based Catalysts for Selective Hydrogenation of Nitroarenes to Anilines. *Science* **2013**, *342*, 1073–1076. [CrossRef]
49. Jagadeesh, R.V.; Junge, H.; Beller, M. Green synthesis of nitriles using non-noble metal oxides-based nanocatalysts. *Nat. Commun.* **2014**, *5*, 4123. [CrossRef]
50. Jagadeesh, R.V.; Natte, K.; Junge, H.; Beller, M. Nitrogen-Doped Graphene-Activated Iron-Oxide-Based Nanocatalysts for Selective Transfer Hydrogenation of Nitroarenes. *ACS Catal.* **2015**, *5*, 1526–1529. [CrossRef]
51. Geniès, L.; Faure, R.; Durand, R. Electrochemical reduction of oxygen on platinum nanoparticles in alkaline media. *Electrochim. Acta* **1998**, *44*, 1317–1327. [CrossRef]
52. Wu, J.; Xia, F.; Pan, M.; Zhou, X.-D. Oxygen Reduction Reaction on Active and Stable Nanoscale TiSi2Supported Electrocatalysts. *J. Electrochem. Soc.* **2012**, *159*, B654–B660. [CrossRef]
53. Schmidt, T.J.; Stamenkovic, V.; Arenz, M.; Markovic, N.; Ross, P. Oxygen electrocatalysis in alkaline electrolyte: Pt(hkl), Au(hkl) and the effect of Pd-modification. *Electrochim. Acta* **2002**, *47*, 3765–3776. [CrossRef]
54. Sun, Z.; Yuan, H.; Liu, Z.; Han, B.; Zhang, X. A Highly Efficient Chemical Sensor Material for H_2S: α-Fe_2O_3 Nanotubes Fabricated Using Carbon Nanotube Templates. *Adv. Mater.* **2005**, *17*, 2993–2997. [CrossRef]
55. Matanovic, I.; Artyushkova, K.; Atanassov, P. Understanding PGM-free catalysts by linking density functional theory calculations and structural analysis: Perspectives and challenges. *Curr. Opin. Electrochem.* **2018**, *9*, 137–144. [CrossRef]
56. Zhang, G.; Yang, X.; Dubois, M.; Herraiz, M.; Chenitz, R.; Lefèvre, M.; Cherif, M.; Vidal, F.; Glibin, V.P.; Sun, S.; et al. Non-PGM electrocatalysts for PEM fuel cells: Effect of fluorination on the activity and stability of a highly active NC_Ar + NH3 catalyst. *Energy Environ. Sci.* **2019**, *12*, 3015–3037. [CrossRef]
57. Yu, X.; Lai, S.; Xin, S.; Chen, S.; Zhang, X.; She, X.; Zhan, T.; Zhao, X.; Yang, D. Coupling of iron phthalocyanine at carbon defect site via π-π stacking for enhanced oxygen reduction reaction. *Appl. Catal. B Environ.* **2020**, *280*, 119437. [CrossRef]
58. Mata, V.R.; González-Domínguez, J.M.; Benito, A.M.; Maser, W.K.; García-Bordejé, E. Reduced Graphene Oxide Aerogels with Controlled Continuous Microchannels for Environmental Remediation. *ACS Appl. Nano Mater.* **2019**, *2*, 1210–1222. [CrossRef]
59. Paulus, U.; Wokaun, A.; Scherer, G.; Schmidt, T.J.; Stamenkovic, V.; Markovic, N.; Ross, P. Oxygen reduction on high surface area Pt-based alloy catalysts in comparison to well defined smooth bulk alloy electrodes. *Electrochim. Acta* **2002**, *47*, 3787–3798. [CrossRef]
60. Tuci, G.; Zafferoni, C.; Rossin, A.; Milella, A.; Luconi, L.; Innocenti, M.; Phuoc, L.T.; Duong-Viet, C.; Pham-Huu, C.; Giambastiani, G. Chemically Functionalized Carbon Nanotubes with Pyridine Groups as Easily Tunable N-Decorated Nanomaterials for the Oxygen Reduction Reaction in Alkaline Medium. *Chem. Mater.* **2014**, *26*, 3460–3470. [CrossRef]